Impact of Well Number on High-Efficiency Strain-Balanced Quantum-Well Solar Cells

Roger E. Welser, Stephen J. Polly, Brandon M. Bogner, and Seth M. Hubbard

***Abstract*—The addition of lower energy-gap InGaAs quantum wells to the depletion region of GaAs solar cells is an established approach to enhance photovoltaic performance by extending infrared collection. However, maintaining a high open-circuit voltage (V_{oc}) when including quantum wells has proven more challenging. In this article, we report on high-efficiency ($\eta > 23.5\%$ AM0) strain-balanced quantum well (SBQW) solar cells with increased current output and efficiency while maintaining the same high open-circuit voltage of baseline devices without quantum wells ($V_{oc} > 1.02$ V). The single-junction GaAs-based device structures discussed herein employ a radiation-tolerant, n-i-p front-junction architecture and include both an InGaP heterojunction (HJ) emitter and in most cases an underlying AlGaAs distributed Bragg reflector. The impact of well number on photovoltaic device characteristics is described using an analytical model that assumes current collection, radiative recombination, and nonradiative recombination all increase with well number and are additive to the baseline cell. The highest V_{oc} and efficiency SBQW devices employ shallow 9.2 nm $In_{0.07}Ga_{0.93}As$ quantum wells and 11.5 nm $GaAs_{0.90}P_{0.10}$ barrier layers to maintain strain balancing. Increasing the indium composition in the wells from 7% to 10% to form deeper wells requires a thicker strain-balancing barrier layer and results in an apparent increase in radiative recombination and decreased V_{oc}. Single-junction high-efficiency SBQW device performance is also demonstrated in thinner base-layer structures with graded HJs—device structures suitable for inclusion in radiation-tolerant multi-junction structures.**

***Index Terms*—Bragg gratings, III-V and concentrator PV, quantum well devices, radiation effects, strain control.**

I. Introduction

After many years of research and development, high-efficiency, single-junction, GaAs-based solar cells incorporating InGaAs quantum wells have recently been reported with one-sun open-circuit voltage (V_{oc}) greater than 1.02 V [1], [2], [3], [4], [5], [6]. These high-efficiency strain-balanced quantum well (SBQW) solar cell devices were achieved by improving the design and careful optimization of growth in the SBQW region, all while employing high-performance GaAs baseline cells. In this article, we reexamine the effect of well number on SBQW photovoltaic device performance in light of these recent technical advances [7].

Adding quantum wells to the junction depletion region of a III-V solar cell is a well-established device design for enhancing current collection. However, both radiative and nonradiative recombination within the quantum well region can, at the same time, degrade V_{oc} and fill factor (FF) performance. The impact of adding quantum wells on the overall efficiency is a tradeoff of these competing effects, and can be described using a simple analytical device model. Past work on GaAs-based SBQW solar cells has typically been limited by nonradiative recombination in the wells and in the baseline cell, resulting in low efficiency performance and V_{oc} values of less than 1 V [1], [7], [8].

In this article, we demonstrate high-efficiency III-V solar cells combining an SBQW absorber with both an underlying distributed Bragg reflector (DBR) and a wide bandgap heterojunction (HJ) emitter. The best cells on structures employing 30 pairs of shallow $In_{0.07}Ga_{0.93}As$ wells and $GaAs_{0.90}P_{0.10}$ barriers yield an AM0 efficiency greater than 23.5%, with a higher current and efficiency than a baseline structure without wells, while maintaining the same high open-circuit voltage. This is a clear demonstration of a quantum well structure increasing the overall efficiency of a GaAs-based solar cell with a high open–circuit voltage ($V_{oc} > 1.02$ V) while simultaneously using a radiation-tolerant, front-junction device structure. Moreover, the realization of GaAs-based SBQW solar cells with enhanced J_{sc} and minimal V_{oc} reduction opens a promising pathway for improving the performance of multijunction devices [2], [4], [5].

Analysis of the impact of well number on the underlying diode parameters of our SBQW devices indicates that the impact of radiative recombination in the shallow-well structures is negligible, maintaining V_{oc} even with the addition of 30x or more wells. On the other hand, deeper-well structures with a higher indium content, which also require thicker strain-balancing barrier layers, exhibit a higher radiative recombination coefficient in the well region and lower V_{oc} values. All structures exhibit a linear increase in nonradiative recombination within the depletion region with increasing well number, resulting in a small degradation in the FF.

We have also fabricated and characterized shallow-well structures with a thinner base layer. The combination of a thin base layer, high-performance back reflector, and SBQW absorber in the junction depletion region was recently demonstrated to

Manuscript received 4 July 2022; revised 8 September 2022 and 11 October 2022; accepted 13 October 2022. Date of publication 2 November 2022; date of current version 12 January 2023. This work was supported by the U.S. Government. *(Corresponding author: Roger E. Welser.)*

Roger E. Welser was with the Magnolia Optical Technologies, Inc., Woburn, MA 01801 USA. He is now an Independent Consultant, Providence, RI 02906 USA (e-mail: roger.e.welser@gmail.com).

Stephen J. Polly, Brandon M. Bogner, and Seth M. Hubbard are with the NanoPower Research Laboratories, Rochester Institute of Technology, Rochester, NY 14623 USA (e-mail: sjpvpr@rit.edu; bxbnprl@rit.edu; smhsps@rit.edu).

Color versions of one or more figures in this article are available at https://doi.org/10.1109/JPHOTOV.2022.3216235.

Digital Object Identifier 10.1109/JPHOTOV.2022.3216235

This work is licensed under a Creative Commons Attribution 4.0 License. For more information, see https://creativecommons.org/licenses/by/4.0/

minimize radiation-induced degradation in short-circuit current density ($J_{\rm sc}$) in both single- and multijunction devices [9], [10]. To minimize radiation-induced $V_{\rm oc}$ degradation, the thinner base layer structures employed in this article include compositionally graded HJ window and emitter layers. The built-in fields generated by the compositional grades are designed to minimize the impact of radiation-induced surface recombination velocity degradation, which has recently been identified as a principal driver of $V_{\rm oc}$ degradation in state-of-the-art III-V solar cells [11]. Analysis of the collection efficiency in these thinner-base SBQW devices indicates that the wells contribute to enhanced $J_{\rm sc}$ not only through extended infrared collection but also from enhanced collection above the GaAs absorption band edge. High voltage performance ($V_{\rm oc} \sim 1.02$ V) has also been obtained in the thinner-base SBQW structures with graded HJs, highlighting the promise of using SBQWs in radiation-tolerant III-V solar cell designs.

II. Analytical Device Model

A simple analytical device model is used to characterize SBQW solar cell performance by assuming the incorporation of wells contributes to both photogenerated current collection and injected current, and that these contributions scale with the number of quantum well layers ($M_{\rm qw}$) [1]. Following the standard analytical model, the solar cell current-voltage (*J–V*) characteristics are assumed to be a balance between the photogenerated short-circuit current density ($J_{\rm sc}$) and injected dark diode current, which is in turn assumed to be the sum of two independent diodes with different voltage dependencies [11], [12]:

$$J = J_{\rm sc} - J_{01}\left\{e^{([qV+JR_{\rm series}]/kT)} - 1\right\} - J_{02}\left\{e^{([qV+JR_{\rm series}]/2kT)} - 1\right\} - \frac{V + JR_{\rm series}}{R_{\rm shunt}} \quad (1)$$

where J_{01} and J_{02} are the n = 1 and n = 2 reverse saturated current densities, q is the electron charge, k is Boltzmann's constant and, T is the temperature, and V is the voltage at the junction. Equation (1) is solved iteratively in this article to fit experimental *J–V* curves which can be influenced by both series resistance ($R_{\rm series}$) and shunt resistance ($R_{\rm shunt}$). Excellent R^2 fit parameters near unity are typically obtained. Note also that (1) assumes that the ideality factor (n) of the space charge recombination component is fixed at $n = 2$, a reasonable assumption for the GaAs-based diode considered in this article, but which could be generalized as needed for InGaP-based cells or other materials [13].

Following the work of Peter Blood [14], the extended infrared absorption of a quantum well solar cell is characterized in terms of the fraction of the light absorbed per layer. Specifically, we define a well collection efficiency (WCE) parameter to quantify the fraction of available photons absorbed and collected by each well. The total $J_{\rm sc}$ from a quantum well solar cell is then the sum of the $J_{\rm sc}$ generated in the baseline cell ($J_{\rm sc}^B$) and that generated in the quantum well region:

$$J_{\rm sc} = J_{\rm sc}^B + \left[1 - (1 - {\rm WCE})^{M_{qw}}\right] J_{\rm sc,ava}^{\Delta\lambda{\rm edge}} \quad (2)$$

where ($J_{\rm sc,ava}^{\Delta\lambda{\rm edge}}$) is the short-circuit current density available given perfect collection in the relevant solar spectrum between the absorption edges of the baseline cell ($\lambda_{\rm base,edge}$) and the quantum well region ($\lambda_{\rm qw,edge}$). As absorption in each overlying well will reduce the light available to underlying wells, the $J_{\rm sc}$ in (2) saturates at higher $M_{\rm qw}$ values, which becomes an important consideration when projecting the impact of well number on overall efficiency performance. Equation (2) also effectively assumes that the contribution from the wells is limited to photons with energies below the band gap of the baseline cell, an assumption that breaks down as the baseline cell is thinned, as will be discussed later in this article. Nevertheless, (2) can still work as an effective empirical model of the impact of well number on $J_{\rm sc}$, either by adding an additional term to describe the available unabsorbed above-band photocurrent or, as done in this article, by empirically increasing the WCE parameter to describe the total $J_{\rm sc}$ in SBQW structures with optically-thin base layers.

Both nonradiative and radiative processes contribute to the dark current of III-V semiconductor diodes, and these processes can have different voltage dependences. Nonradiative dark current processes can follow either an $n = 1$ or $n = 2$ voltage dependence, contingent upon the location of the recombination within the device. Nonradiative events in the quasi-neutral regions of the device contribute to the $n = 1$ component, while nonradiative events within the junction depletion region contribute to the $n = 2$ space charge recombination component of the diode dark current. Radiative processes have an $n = 1$ voltage dependence, both in the quasi-neutral region of the baseline cell and in the quantum well region [15]. Radiative emissions from the quantum well region have been previously shown to dominate the dark diode characteristics of quantum well solar cells at high bias levels, even when nonradiative processes limit 1-sun photovoltaic device performance [16], [17].

In this article, radiative recombination in each quantum well layer is described mechanistically in terms of carrier recombination via the use of a two-dimensional (2-D) radiative recombination coefficient ($B_{\rm rad,2D}$) [14]. Assuming evenly emitting wells, the $n = 1$ component (J_{01}) will increase linearly with well number:

$$J_{01} = J_{01}^B + qN_{2D}^2 e^{(-E_g^{qw}/kT)} B_{\rm rad,2D} M_{qw} \quad (3)$$

where J_{01}^B is the n = 1 reverse saturation current component of the baseline cell and E_g^{qw} is the effective energy gap of the quantum well region ($E_g^{qw} = hc / \lambda_{qw,{\rm edge}}$). We further assume that the carrier density in each layer can be characterized by a fixed 2-D carrier concentration $N_{2D} = 1 \times 10^{12}$ cm^{-2}.

Since the quantum wells reside within the junction depletion region, the nonradiative recombination from the quantum well region is assumed to add incrementally only to the $n = 2$ component. Specifically, we assume that that the $n = 2$ saturation current density (J_{02}) scales with well number:

$$J_{02} = J_{02}^B + qN_{2D} e^{(-E_g^{qw}/2kT)} A_{\rm SCR,2D} M_{qw} \quad (4)$$

where J_{02}^B is the $n = 2$ reverse saturation current component of the baseline cell, and $A_{\rm SCR,2D}$ is the nonradiative space charge

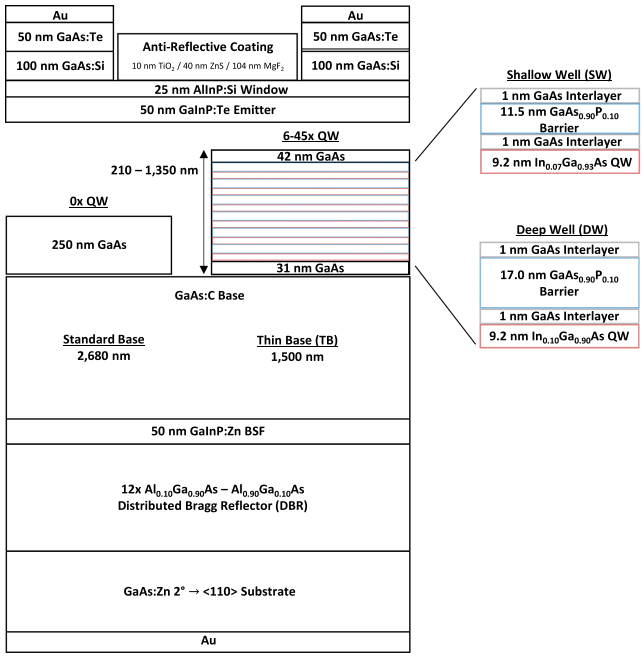

Fig. 1. Simplified schematic of the basic SBQW solar cell structure investigated in this study. In addition to well number, different device structures varied in $In_xGa_{1-x}As$ well composition (x), $GaAs_{0.90}P_{0.10}$ barrier thickness, base layer thickness, and the use of compositional grades in the emitter and window layers, as given in Table I.

recombination coefficient. The $A_{SCR,2D}$ coefficient is expected to increase with trap density, both within the well and barrier layers and at each well-barrier interface. Note also that Equations (2)–(4) imply that J_{sc}, J_{01} and J_{02} are all sensitive not only to well number, but also to the quantum well region absorption edge via E_g^{qw}.

III. Device Structures and Experimental Details

Fig. 1 summarizes the n-i-p front-junction device structure used in this study to probe the impact of well number on photovoltaic device properties. Unless otherwise noted, a p-type AlGaAs DBR is incorporated below the p-type GaAs base layer. The thickness of the 12 pairs of $Al_{0.10}Ga_{0.90}As$ and $Al_{0.90}Ga_{0.10}As$ layers in the DBR are tuned to produce a region of high reflectance centered at approximately 900 nm. Wide band gap n-type InGaP and AlInP are employed in the emitter and window layers, nominally lattice matched to the underlying GaAs and forming an HJ. The SBQW region is inserted into the junction depletion region, surrounded on both sides by intrinsic layers of GaAs without intentional doping. The $In_xGa_{1-x}As$ quantum wells are also undoped and strain balanced with $GaAs_{0.90}P_{0.10}$ barrier layers [18], [19]. Thin 1 nm GaAs transition layers are inserted at each As-P interface in the well region. This barrier layer design and interface sequence was found to facilitate the growth of high-quality quantum well regions [5], [20], [21]. Both X-ray diffraction measurements on calibration structures and *in situ* Laytec EpiCurveTT wafer curvature measurements on each device structure were used to confirm the SBQW region is effectively strain-balanced, typically exhibiting a slight compressive strain (< 700 ppm).

TABLE I
Summary of the Key Differences Between the Three Different Flavors of SBQW Solar Cell Structures Investigated in This Study. The Well Thickness is Fixed at 9.2 nm, and All Three Structures Include an Underlying AlGaAs DBR and an InGaP HJ Emitter as Shown in Fig. 1

Device Structure	Well In Content (%)	Barrier Thickness (nm)	$\lambda_{qw,edge}$ (nm)	Base Layer Thickness (nm)	Graded Emitter & Window
SW	7	11.5	925	2,680	No
DW	10	17.0	945	>2,680	No
SW-TB	7	11.5	925	1,500	Yes

Three different flavors of the basic structure shown in Fig. 1 are investigated, with key structure differences given in Table I. Two flavors of device structures use relatively shallow wells (SW) with $x \sim 7\%$, yielding an absorption edge at 925 nm. A separate group of device structures employs deeper wells (DW) with $x \sim 10\%$, yielding an absorption edge at 945 nm. All the wells are nominally 9.2 nm thick. The thickness values of the intrinsic layers above and below the SBQW region are fixed; thus the total intrinsic region thickness increases with well number.

The final set of device structures combines the SW design with a thinner base layer (SW-TB). Reducing the base thickness limits the effects of radiation-induced minority carrier diffusion length degradation, creating a more radiation tolerant design. This normally comes at the cost of reduced photon absorption and decreased current density; however, in this case, the simultaneous addition of a thicker intrinsic region incorporating SBQWs allows nearly identical above-band collection to a thick-base design without SBQWs. The SW-TB structures also employ compositional grades in the InGaP emitter and AlInP window layers. The $\sim 5\%$ change in indium composition in each layer is expected to result in an energy band gradient of ~ 3 to 4 kT. The compositional grade can result in a residual strain in each layer, but well below the calculated critical thickness.

All devices were grown on offcut p-doped 2" GaAs (100) substrates using a 3x2" Aixtron close-coupled showerhead metal organic vapor phase epitaxy (CCS-MOVPE) reactor. Standard group III precursors of trimethylindium, trimethylgallium, and trimethylaluminum were used, along with arsine and phosphine group V sources. Disilane and diethyltellurium were used as the n-type dopants, while p-type doping was achieved both via the control of the V/III ratio and external p-type dopant sources (carbon tetrachloride, diethylzinc). Materials were grown at approximately 650 °C (substrate surface temperature as measured with an *in situ* Laytec emissivity corrected pyrometer system). V/III ratios used were typically between 50–200 depending on material. Growth rates for most layers were between 1 and 2 μm/hr.

A total of 12 1×1 cm^2 cells were fabricated on each 2" wafer in a series of process lots using conventional III/V processing techniques. The three best cells from each wafer were used to characterize photovoltaic device performance on each structure in the process lot. Contact lithography was used to define the front contact metal grid regions. These were electroplated with

5 nm Ni and 1.6 μm Au for n-type ohmic contacts, or 5 nm Zn and 2 μm Au for p-type ohmic contacts, using commercial plating solutions purchased from Transene. Contact resistances of $<5 \times 10^{-5}$ Ω/cm^2 were typical, as extracted from transfer length method (TLM) measurements. Contact lithography was then used to define the active areas which were isolated using a wet chemical etch. All samples were then coated with an antireflection coating comprised of 10 nm of TiO_2 (atomic layer deposition), 40 nm ZnS and 105 nm MgF_2 (thermal evaporation), which was optimized to minimize surface reflection loss from 300 to 1000 nm.

External quantum efficiency (EQE) measurements were taken using a Newport IQE 200 quantum efficiency measurement system which was calibrated using both Newport silicon (Model 818-UV-L) and Newport germanium (Model 818-IR-L) reference detectors. AM0 (1-sun) illuminated *I–V* measurements were performed using a dual source 18 kW solar simulator system custom built by TS space systems. The system was calibrated using $InGaP_2$ ($E_g = 1.85$ eV) and GaAs ($E_g = 1.42$ eV) cells calibrated by the National Renewable Energy Laboratory. The spectral match between RIT AM1.5G/AM0 and ASTM AM1.5G/AM0 is nearly unity from 350 to 1200 nm with exception of out of range points between 600–700 nm [22]. During the measurement, the samples were placed on a temperature-controlled chuck set at 25 °C. Illuminated diode behavior was measured using a Keithley 2400 source meter.

IV. Results

Fig. 2(a) compares AM0 illuminated *J–V* curves from the highest-efficiency cell from this study to a representative baseline cell. These champion cell results were achieved on an SW structure with 30 pairs of strain-balanced $In_{0.07}Ga_{0.93}As$ wells and $GaAs_{0.90}P_{0.10}$ barriers. The J_{sc} is significantly higher compared to the baseline cell ($\Delta J_{sc} \sim 2.4$ mA/cm^2) and the V_{oc} is identical (~ 1.02 V). Despite a slightly lower FF on the 30*x* well cell (82.7% vs. 85.0%), the overall AM0 efficiency is notably higher (23.6% versus 22.7%). The measured EQE spectrum, shown in Fig. 2(b), reveals substantial extended infrared collection from the quantum well region, exceeding 40% at a wavelength of 900 nm. This is a clear demonstration of a quantum well structure increasing the overall efficiency of a high-voltage GaAs-based solar cell.

The solid shapes in Fig. 2(a) represent measured data points, while the solid lines are a two-diode fit of the measured *J–V* curve. The extracted photovoltaic and diode parameters are shown inset. The magnitude of the $n = 1$ component of the dark diode current (J_{01}) is comparable in the two cells. On the other hand, the $n = 2$ component of the diode current (J_{02} value) is $\sim 2.5x$ higher compared to the 0*x* well SW baseline structure, indicating an increase in space charge recombination as wells are added. To better assess the impact of well number as a whole, Figs. 3 and 4 plot out the photovoltaic and diode parameters from the best three cells on each wafer from all SW and SW-TB structures as a function of well number. These plots capture some of the expected cell-to-cell variation across the wafer, as well

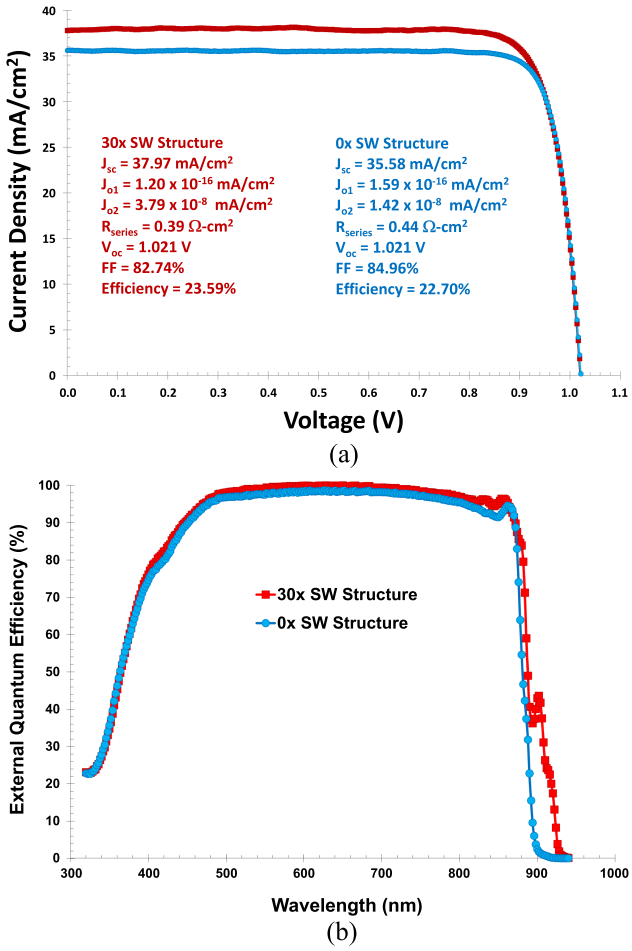

Fig. 2. Comparison of (a) illuminated AM0 current-voltage characteristics and (b) EQE curves of SW structures with 30*x* wells and no (0x) wells. *J–V* fit parameters are shown inset.

as variations between growth and fabrication lots. The dashed lines in Figs. 3 and 4 are best fits of the extracted diode and photovoltaic parameters using the analytical model described by (1)–(4).

Very little variation in the $n = 1$ component (J_{01}) of the SW and SW-TB structures is observed in Fig. 3(a) as the well number increases. These results imply that radiative recombination in the wells is not playing a significant role in limiting the dark diode current of the SW structures. Instead, nonradiative recombination in the baseline cell (J_{01}^B) dominates. For reference, the modeled dashed line in Fig. 3(a) assumes an effective radiative recombination coefficient in the wells ($B_{\mathrm{rad,2D}} = 8.5 \times 10^{-5}$ cm^2/s) that is lower than that inferred from many earlier reports on SBQW solar cells [1], but which also represents an upper bound of possible values that can reasonably fit the experimental data.

On the other hand, a notable increase in the $n = 2$ component (J_{02}) is observed in Fig. 3(b) as wells are added to the structure. This increase in the $n = 2$ component of the dark diode current is associated with an increase in recombination in the junction depletion region. As detailed in (4), an increase in space charge recombination is expected when adding quantum wells to the

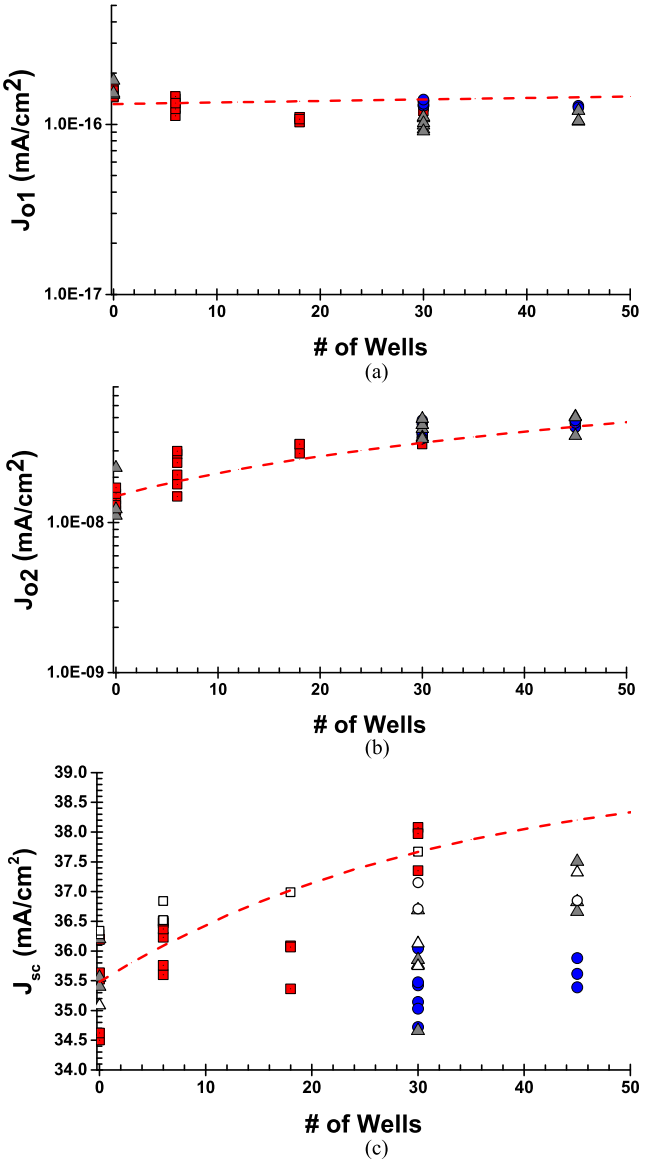

Fig. 3. Measured (solid shapes) and modeled (dashed line) variation in (a) and (b) diode parameters (J_{01} and J_{02}) and (c) short-circuit current density (J_{sc}) of shallow-well structures as a function of well number. Different shapes and colors correspond to different fabrication lots (SW = squares and circles; SW-TB = triangles). The integrated J_{sc} from the measured EQE spectrum is also shown in (c) as open shapes.

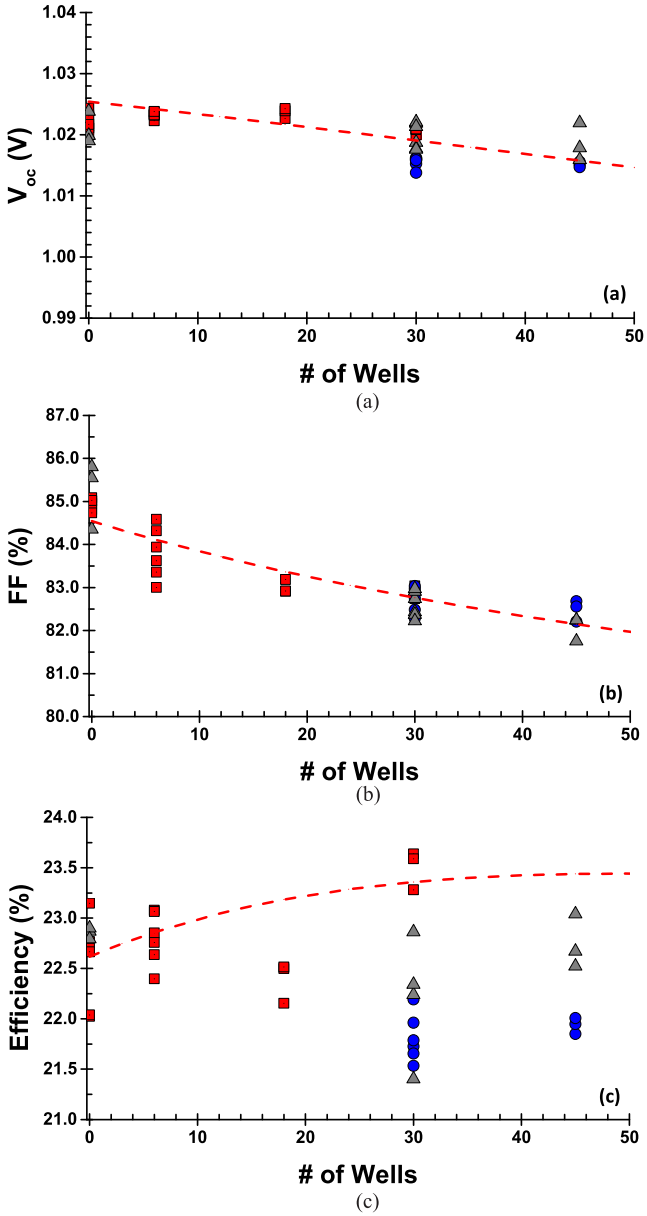

Fig. 4. Measured (solid shapes) and modeled (dashed line) variation in photovoltaic device parameters (a) V_{oc}, (b) FF and (c) AM0 efficiency of shallow-well structures as a function of well number. Different shapes correspond to different fabrication lots (SW = squares and circles; SW-TB = triangles).

depletion region. The modeled dashed line in Fig. 3(b) assumes a nonradiative space charge recombination coefficient ($A_{SCR,2D} = 8.4 \times 10^5$ s^{-1}) that is comparable to that inferred from our earlier work on strained quantum well solar cells, which was in turn lower than prior work on strain-balanced devices [1].

Fig. 3(c) summarizes the impact of well number on the short-circuit current density (J_{sc}), plotting both the integrated J_{sc} and the measured J_{sc} on the three best cells from each structure, along with the modeled J_{sc} dependence on well number. The measured J_{sc} exhibits a fair degree of variation across the wafer and between fabrication lots, but in most structures the values obtained on the best cells approach the integrated J_{sc} derived from the measured EQE spectrum. The measured J_{sc} is expected to be 4% lower than the integrated J_{sc} due to grid shadowing which does not impact EQE measurements. The dashed line shown in Fig. 3(c) is the modeled variation in J_{sc} assuming that the absorption from each well is 3.0% of the available photocurrent between the GaAs and quantum well absorption edges (i.e., 875 and 925 nm) and that the baseline cell J_{sc}^{B} can be described with a square 95.25% EQE profile and a UV cutoff wavelength of 360 nm. As will be discussed in more detail later, this WCE value of 3% is higher than that inferred when considering only extended IR collection. Enhanced collection above the GaAs band edge is effectively contributing to the WCE value in Fig. 3(c), as both the SW and SW-TB structures employ optically-thin base layers. Variations in the performance of the

antireflective coating and DBR structures, particularly on the second SW process lot, also add to the uncertainty in the fit of the total J_{sc} dependence on well number.

Next, (1) was used to generate J–V curves assuming the modeled variations in J_{01}, J_{02}, and J_{sc} summarized by the dashed lines in Fig. 3. The resulting modeled variation in photovoltaic device properties as a function of well number is compared to measured values in Fig. 4. In particular, Fig. 4(a) summarizes the impact of well number on the open-circuit voltage (V_{oc}) from the three best devices on each wafer. The observed decrease in V_{oc} with well number in the SW and SW-TB structures is small. In fact, the V_{oc} is 1.015 V or higher on all of the best cells in all of the SW and SW-TB structures, even when the well number is increased to 45x.

The FF exhibits a small, but notable reduction as the number of wells increases. The FF on all the SW and SW-TB devices is largely dominated by the $n = 2$ component, decreasing as the J_{02} values increase. The observed variation in FF seen in Fig. 4(b) mirrors the observed variation in extracted J_{02} depicted in Fig. 3(b). The modeled variation in FF is driven by the modeled increase in J_{02}.

Fig. 4(c) summarizes the impact of well number on the measured efficiency from the three best devices on each wafer. As previously noted, the efficiency values of the best cells from the 30x well structure are notably higher than the efficiency of the best cells from the baseline structure with no (0x) wells. However, there is significant variation in the efficiency values, particularly from lot to lot, as variations in the AR coatings strongly impacts both the J_{sc} and the efficiency. As a whole, the calibrated analytical model projects the overall efficiency should increase with well number, as the fitted increase in J_{sc} is larger than the fitted increases in J_{01} and J_{02} that slightly degrade FF and V_{oc}. However, this projected increase in efficiency saturates with increasing well number, with near negligible efficiency benefits for increasing the well number greater than $\sim 30x$.

As an alternative to increasing well number as a means to increase J_{sc}, we have also explored the photovoltaic performance of DW structures that extend collection further into the IR. Fig. 5 summarizes the experimentally observed impact of well composition on photovoltaic device results by comparing similar structures employing shallow 7% InGaAs wells (SW and SW-TB in red) and deeper 10% InGaAs wells (DW in blue). As expected, increasing the indium composition in the well shifts the absorption edge from the quantum well region further into the infrared, as illustrated with the EQE comparison shown on Fig. 5(a) for two 30x well structures, identical except for the well composition and barrier thickness, grown back-to-back and processed together. Note also that the EQE is nearly identical in the two structures at wavelengths shorter than 925 nm.

The benefit of the absorption edge shift from approximately 925 nm in the SW structures to 945 nm in the DW structures is small in terms of overall current collection – $\Delta J_{sc,integrated} \sim 0.2$ mA/cm^2 in Fig. 5(a), and it comes with a significant cost in terms of a degradation in open-circuit voltage. The measured open-circuit voltage of the DW structures decreases with increasing well number at a much higher rate than in the SW and SW-TB structures, as depicted in Fig. 5(b). Comparison

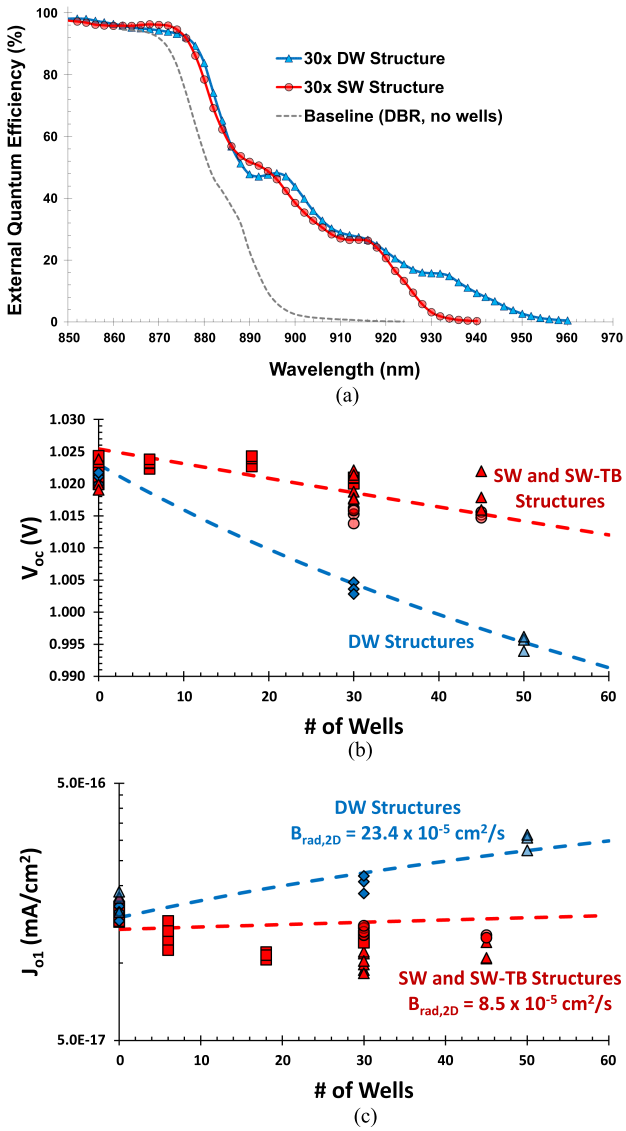

Fig. 5. Comparison of the (a) EQE from shallow- and deep-well structures, along with (b) and (c) measured (solid shapes) and modeled (dashed line) variation in V_{oc} and J_{01} as a function of well number. Different shapes in (b) and (c) correspond to different fabrication lots of SW and SW-TB structures as in Figs. 3 and 4, with data from DW structures added in blue.

of the extracted diode components indicates that the differences in V_{oc} between the DW and SW structures is largely being driven by differences in the $n = 1$ component. Fig. 5(c) compares the variation in J_{01} of DW structures to SW and SW-TB structures as a function of well number. The J_{01} values of the DW structures increase notably with increasing well number, whereas the J_{01} of the SW structures has a very weak dependence, as previously noted. The impact of the smaller effective energy gap of the DW, $E_g^{qw} = 1.312$ eV versus 1.341 eV, does not by itself come close to capturing the magnitude of the observed increase in J_{01} values. Instead, the implied radiative recombination coefficient, $B_{rad,2D}$, is substantially higher (2.75x) in the DW structures. While the $n = 2$ current component is also slightly higher in the DW structures, the magnitude of this increase relative to the SW structures is consistent with the shift in E_g^{qw}. The implied

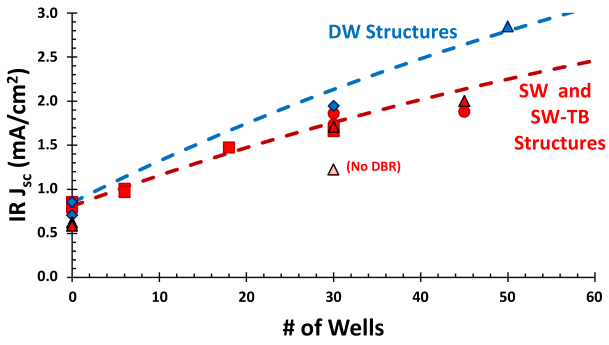

Fig. 6. Measured (solid shapes) and modeled (dashed lines) variation in the integrated infrared J_{sc} ($>$ 870 nm) as a function of well number for shallow- and deep-well structures. Different shapes and colors correspond to different fabrication lots and structures as in Fig. 5.

nonradiative space charge recombination coefficient, $A_{SCR,2D}$, is comparable in all three structures, varying by less than 15% between the DW and SW structures. As will be discussed later, the implied differences in $B_{rad,2D}$ correlate not only with well depth, but with $GaAs_{0.90}P_{0.10}$ barrier layer thickness, as the DWs require thicker barriers, as given in Table I.

While a significant increase in $B_{rad,2D}$ is required to account for the higher J_{01} and lower V_{oc} observed in the DW structures, the expected increase in $J_{sc,ava}^{\Delta\lambda edge}$ due to the extended absorption edge is sufficient to account for the small J_{sc} increase seen in the DW structures. Fig. 6 compares the integrated infrared J_{sc} of the DW and SW structures. By focusing only on collection at wavelengths longer than 870 nm, this integrated infrared IR J_{sc} metric captures the impact of wells on extending infrared collection independent of the effects of limited absorption above the GaAs band edge in optically-thin structures. As expected, the DW structures provide a slight boost in integrated J_{sc}, especially as the number of wells increases. The dashed lines in Fig. 6 both assume a WCE value of 1%, but the longer absorption edge of the DW structures (945 nm versus 925 nm) results in more available J_{sc}, e.g., the $J_{sc,ava}^{\Delta\lambda edge}$ term in (2). Fig. 6 also shows the integrated IR $J_{sc\ c}$ from a 30-well SW-TB structure without a DBR. This structure without an underlying DBR has a notable lower IR J_{sc}, with an implied WCE of ~0.5%, half that of the structures with a DBR. This finding is consistent with the transparent DBR structures reflecting unabsorbed IR photons back into the SBQW absorber region and effectively doubling the collection efficiency from the wells via a second pass of unabsorbed photons.

In summary, we observe that our 9.2 nm thick InGaAs wells absorb and collect ~0.5% of the available infrared photons per well, and that this WCE value is doubled to ~ 1% after adding a high-performance DBR below the absorber regions. On the other hand, we observe WCE values as high as 3% when considering the total J_{sc} from the same set of SBQW devices, as shown in Fig. 3(c). This discrepancy can be at least partially accounted for by enhanced absorption above the GaAs band edge in structures with optically-thin GaAs base layers. This effect is particularly evident in our SW-TB structures, an example of which is shown in Fig. 7.

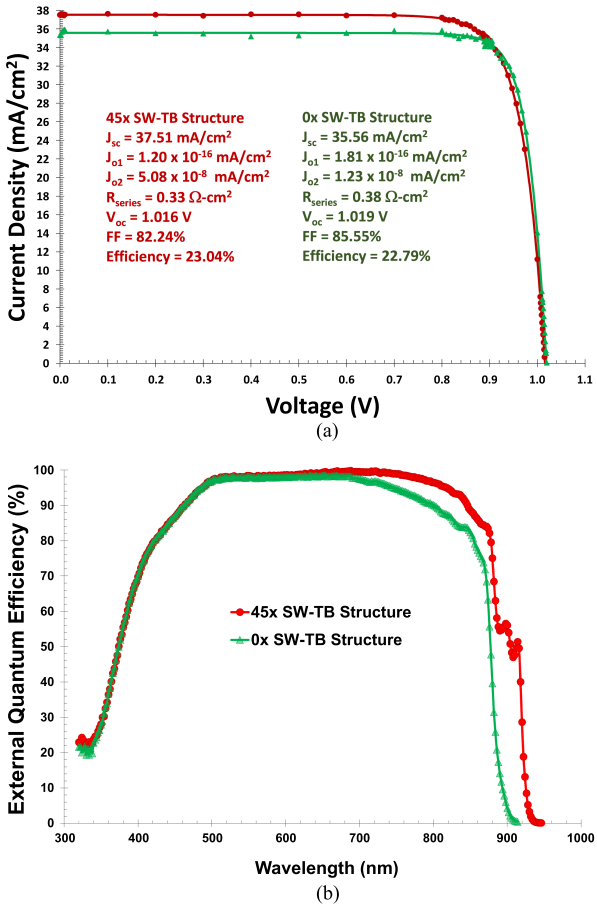

Fig. 7. Comparison of (a) illuminated AM0 current-voltage characteristics and (b) EQE curves of shallow-well structures with a thinner base layer (SW-TB) with 45x wells and no (0x) wells. *J–V* fit parameters are shown inset.

As detailed in Table I, our SW-TB structures combine a shallow-well SBQW absorber with both a thinner base layer and a compositionally graded HJ. Both structural changes are incorporated to improve the potential radiation tolerance of the device. As summarized in Fig. 7(a), the best SW-TB cell with 45*x* well-barrier pairs has a substantially higher current than a SW-TB baseline with no wells ($\Delta J_{sc} \sim 2.0$ mA/cm^2). Moreover, this 45*x* well SW-TB device also has a high voltage ($V_{oc} \sim$ 1.016), almost identical to the thin-base baseline device. As with the SW device comparison shown in Fig. 2, adding wells to the baseline SW-TB structure results in a measurably lower FF, but the increase in J_{sc} and comparable V_{oc} outweigh the decrease in FF in the Fig. 7 comparison, yielding a slightly higher overall efficiency (23% versus 22.8%).

The higher J_{sc} in the SW-TB structures with thinner GaAs base layers is clearly derived from both extended infrared absorption and enhanced collection above the GaAs band edge, as seen in the EQE comparison in Fig. 7(b). Similar to the thicker SW structures, the addition of 45*x* wells to the SW-TB structure results in substantial extended infrared collection from the quantum well region, with EQE exceeding 50% at wavelengths out to ~915 nm and ~8% @ 925 nm. In addition, collection is enhanced at shorter wavelengths above the GaAs band edge,

with the EQE from the 45x SBQW structure clearly exceeding the SW-TB baseline at wavelengths as short as 690 nm.

Quantitatively, the total integrated $J_{\rm sc}$ of the 45x well structure in Fig. 7(b) is $\sim$2.25 mA/cm^2 higher than the baseline (37.32 mA/cm^2 versus 35.08 mA/cm^2). On the other hand, the IR $J_{\rm sc}$ is $\sim$1.4 mA/cm^2 higher (2.00 mA/cm^2 versus 0.59 mA/cm^2). Collection above the GaAs band edge is thus contributing an additional $\sim$0.85 mA/cm^2 to the total integrated $J_{\rm sc}$. Adding 45 pairs of InGaAs wells and GaAsP barriers in this comparison adds $\sim$1020 nm of absorbing material to the depletion region. Prior projections of the impact of GaAs absorber thickness on $J_{\rm sc}$ [23] predict a near identical boost in $J_{\rm sc}$, suggesting the InGaAs/GaAsP SBQW absorber employed in this article is at least as good as GaAs at collecting photogenerated carriers above the GaAs band edge in structures with an optically-thin base layer.

V. Conclusion

The impact of well number on the photovoltaic device performance of high-efficiency GaAs-based SBQW solar cells is reasonably well described using the simple analytical model defined by (1)–(4). Changes in diode components, J_{01} and J_{02}, are closely fit as increasing linearly with well number using $B_{\rm rad,2D}$ and $A_{\rm SCR,2D}$ coefficients to characterize radiative and nonradiative recombination, respectively. The extended absorption and collection of the moderately thick wells (9.2 nm) considered in this study is closely fit assuming a WCE of 1% per well when coupled with an underlying DBR, with DWs offering a slightly higher $J_{\rm sc}$ due to their longer wavelength absorption edge. This article also clearly demonstrates that adding wells can enhance the collection efficiency above the GaAs band edge in structures with optically-thin base layers. As a result, the WCE value is found to be substantially larger than 1% in optically-thin structures when considering the impact of well number on the total $J_{\rm sc}$.

In both shallow- and deep-well structures, adding wells results in a clear increase in the $n = 2$ component of the diode dark current, which in turn results in a decrease in FF with increasing well number. The $n = 1$ component also increases with well number in DW structures, but is nearly independent of well number in SW structures. As a result, the $V_{\rm oc}$ is also nearly independent of well number in SW structures, but decreases with increasing well number in DW structures. Analysis of these results suggest that radiative recombination plays a reduced role in the SW structures not only due to a higher E_g^{qw}, but also because of a 2.75x reduction in the effective radiative recombination coefficient in SW structures relative to DW structures.

Although the exact cause of the apparent differences in $B_{\rm rad,2D}$ between the SW and DW structures is at present unclear, we note here that there is a correlation with barrier thickness, as DW structures also require the use of thicker $GaAs_{0.90}P_{0.10}$ barrier layers to maintain strain balancing. Prior work on strained quantum well solar cells has discussed the possibility that radiative recombination can be suppressed in thinner barrier structures with reduced carrier overlap in the multiple-quantum-well region [1]. Moreover, classic detailed balance descriptions of radiative recombination in photovoltaic devices [24], [25] highlight how differences in the angular emission profile and/or the wavelength dependence of the emission spectrum of the absorber region can impact the radiative current [26], [27]. From a detailed balanced perspective, we could therefore also postulate that the SW structures may have a more restricted angular emission profile and/or a narrower emission wavelength band compared with the DW structures.

In any event, the combination of increased $J_{\rm sc}$ and high $V_{\rm oc}$ in the SW structures with a limited number of wells ($\sim 30x$) results in a demonstrated increase in efficiency, and our best single-junction cells exhibit an AM0 efficiency greater than 23.5%. In these high-efficiency GaAs-based quantum well devices, decreasing FF has become a key factor limiting further efficiency improvements. The observed degradation in FF with increasing well number results from increasing J_{02} values, which might be mitigated by further improvements in the growth of the wells and their interfaces to reduce $A_{\rm SCR,2D}$, the nonradiative space charge recombination coefficient.

In summary, high-efficiency performance has been demonstrated in advanced GaAs-based solar cells combining a SBQW absorber with both an underlying DBR and a wide band gap HJ. These device structures also employ an n-on-p front-junction similar to that used in space-qualified multi-junction devices. The best single-junction device results, and highest open-circuit voltages, are realized in structures that are carefully strain-balanced, and that employ thinner, shallower $In_{0.07}Ga_{0.93}As$ wells that require $GaAs_{0.90}P_{0.10}$ barriers less than 15 nm in thickness. While slightly different tradeoffs will apply to multi-junction device designs, we expect both beginning-of-life and end-of-life performance could be improved by incorporating device structures similar to those discussed in this study into the GaAs-based subcell of a multi-junction device to increase the overall $J_{\rm sc}$ budget.

References

[1] R. E. Welser et al., "Design and demonstration of high-efficiency quantum well solar cells employing thin strained superlattices," *Sci. Rep.*, vol. 9, Sep. 2019, Art. no. 13955.

[2] M. A. Steiner et al., "High efficiency inverted GaAs and GaInP/ GaAs solar cells with strain-balanced GaInAs/GaAsP quantum wells," *Adv. Energy Mater.*, vol. 11, Dec. 2020, Art. no. 2002874.

[3] A. Fedorenko, S. Polly, B. Bogner, and S. M. Hubbard, "Enhancing open-circuit voltage and efficiency of shallow $in_xGa_{1-x}As$ quantum well GaAS solar cells," in *Proc. IEEE 48th Photovolt. Specialists Conf.*, 2021, pp. 1524–1526.

[4] R. M. France et al., "Triple-Junction solar cells with 39.5% terrestrial and 34.2% space efficiency enabled by thick quantum well superlattices," *Joule*, vol. 6, pp. 1121–1135, May 2022.

[5] S. J. Polly et al., "Growth optimization of InGaP/ GaAS dual junction solar cells with quantum wells and a distributed Bragg reflector," Sep. 2022. [Online]. Available: https://ssrn.com/abstract=4219119 or http://dx.doi.org/10.2139/ssrn.4219119

[6] B. M. Bogner, S. J. Polly, S. M. Hubbard, and R. E. Welser, "Thin, radiation-resilient III-V PV devices utilizing quantum structures and epitaxial light reflectors," in *Proc. IEEE 49th Photovolt. Specialists Conf.*, 2022, Paper C20.

[7] D. B. Bushnell et al., "Effect of well number on the performance of quantum-well solar cells," *J. Appl. Phys.*, vol. 97, Jun. 2005, Art. no. 124908.

[8] I. Sayed and S. M. Bedair, "Quantum well solar cells: Principles, recent progress, and potential," *IEEE J. Photovolt.*, vol. 9, no. 2, pp. 402–423, Mar. 2019.

[9] R. Tatavarti et al., "Radiation hardening of dual junction solar cells," in *Proc. IEEE 47th Photovolt. Specialists Conf.*, 2020, pp. 2258–2261.
[10] S. R. Tatavarti, K. Forghani, A. Wibowo, and R. E. Welser, "Radiation-Induced degrdation mechanisms in thin-film multiple quantum well solar cells with wavelength-selective photonic structures," *IEEE J. Photovolt.*, vol. 12, no. 5, pp. 1192–1197, Sep. 2022.
[11] N. Gruginskie et al., "Electron radiation-induced degradation of GaAs solar cells with different architectures," *Prog. Photovolt. Res. Appl.*, vol. 2020, no. 28, pp. 266–278, Nov. 2019.
[12] C. B. Honsberg and S. G. Bowden, "Photovoltaics education website," 2019. [Online]. Available: www.pveducation.org
[13] J. F. Geisz, M. A. Steier, I. Garcia, S. R. Kurtz, and D. J. Friedman, "Enhanced external radiative efficiency for 20.8% efficient single-junction GaInP solar cells," *Appl. Phys. Lett.*, vol. 103, Jul. 2013, Art. no. 041118.
[14] P. Blood, "On the dimensionality of optical absorption, gain, and recombination in quantum-confined structures," *IEEE J. Quantum Electron.*, vol. 36, no. 3, pp. 354–362, Mar. 2000.
[15] D. C. Johnson et al., "Observation of photon recycling in strain-balanced quantum well solar cells," *Appl. Phys. Lett.*, vol. 90, May 2007, Art. no. 213505.
[16] A. Bessiere et al., "Radiative recombination in strain-balanced quantum well solar cells," in *Proc. IEEE 31st Photovolt. Specialists Conf.*, 2005, pp. 679–682.
[17] R. E. Welser, "Thick-Well quantum-structured solar cells: Design criteria for nano-enhanced absorbers," *Proc. SPIE*, vol. 8620, Feb. 2013, Art. no. 86201C-1.
[18] N. J. Ekins-Daukes, K. Kawaguchi, and J. Zhang, "Strain-balanced criteria for multiple quantum well structures and its signature in X-ray rocking curves," *Cryst. Growth Des.*, vol. 2, no. 4, pp. 287–292, Jul. 2002.
[19] S. J. Polly, C. G. Bailey, A. J. Grede, D. V. Forbes, and S. M. Hubbard, "Calculation of strain compensation thickness for III–V semiconductor quantum dot superlattices," *J. Cryst. Growth*, vol. 454, pp. 64–70, Nov. 2016.
[20] Y. Wen, Y. Wang, and Y. Nakano, "Suppressed indium diffusion and enhanced absorption in InGaAs/GaAsP stepped quantum well solar cell," *Appl. Phys. Lett.*, vol. 100, Feb. 2012, Art. no. 053902.
[21] H. Fujii, Y. Wang, K. Watanabe, M. Sugiyama, and Y. Nakano, "Suppressed lattice relaxation during InGaAs/GaAsP MQW growth with InGaAs and GaAs ultra-thin interlayers," *J. Cryst. Growth*, vol. 352, no. 1, pp. 239–244, Aug. 2012.
[22] S. J. Polly, Z. S. Bittner, M. F. Bennett, R. P. Raffaelle, and S. M. Hubbard, "Development of a multi-source solar simulator for spatial uniformity and close spectral matching to AM0 and AM1.5," in *Proc. IEEE 37th Photovolt. Specialists Conf.*, 2011, pp. 001739–001743.
[23] R. E. Welser, S. J. Polly, A. K. Sood, S. M. Hubbard, and K. H. Montgomery, "Epitaxial reflector structures for high efficiency quantum well solar cells," in *Proc. IEEE 46th Photovolt. Specialists Conf.*, 2019, pp. 2642–2645.
[24] A. Marti, J. L. Balenzategui, and R. F. Reyna, "Photon recycling and Shockley's diode equation," *J. Appl. Phys.*, vol. 82, pp. 4067–4075, Jun. 1997.
[25] U. Rau, "Reciprocity relation between photovoltaic quantum efficiency and electroluminescence emission of solar cells," *Phys. Rev. B*, vol. 76, Aug. 2007, Art. no. 085303.
[26] J. G. J. Adams et al., "Higher limiting efficiencies for nanostructured solar cells," *Proc. SPIE 7597, Phys. Simul. Optoelectron. Devices XVIII*, vol. 7597, Feb. 2010, Art. no. 759705.
[27] R. E. Welser et al., "The physics of high-efficiency thin-film III-V solar cells," in *Solar Cells -New Approaches and Reviews*, L. A. Kosyachenko Ed., London, U.K.: InTech, Oct. 2015. [Online]. Available: https://www.intechopen.com/books/4479